

Pump or coast: The role of resonance and passive energy recapture in medusan swimming performance

Alexander P. Hoover^{1†}, Antonio J. Porras², and Laura A. Miller^{3,4}

¹Department of Mathematics, Tulane University, New Orleans, LA 70118

²Department of Life and Physical Sciences, Fisk University, TN 37208

³Department of Mathematics, University of North Carolina at Chapel Hill, Chapel Hill, NC 27599

⁴Department of Biology, University of North Carolina at Chapel Hill, Chapel Hill, NC 27599

(Received xx; revised xx; accepted xx)

Diverse organisms that swim and fly in the inertial regime use the flapping or pumping of flexible appendages and cavities to propel themselves through a fluid. It has long been postulated that the speed and efficiency of locomotion are optimized by oscillating these appendages at their frequency of free vibration. More recently, work on some fish and insects suggest that the efficiency of locomotion is not maximized through the resonant driving of locomotory organs since the resulting large oscillations generate significant drag. Lumped parameter and 2D fluid-structure interaction models of jellyfish swimming suggest that their swimming speeds and costs of transport are optimized by driving the bell at its natural frequency. These studies have not, however, captured the effects of passive energy recapture whereby the bell is passively propelled through the fluid through its interaction with stopping vortex rings formed during each expansion of the bell. In this paper, we use a three-dimensional implementation of the immersed boundary method to solve the fluid-structure interaction of an elastic oblate jellyfish bell propelling itself through a viscous fluid. The motion is generated through a fixed duration application of active tension to the bell margin, which mimics the action of the coronal swimming muscles. The pulsing frequency is then varied by altering the length of time between the application of applied tension. We find that the swimming speed is maximized when the bell is driven at its resonant frequency. However, the cost of transport is maximized by driving the bell at lower frequencies whereby the jellyfish passively coasts between active contractions through its interaction with the stopping vortex ring. Furthermore, the thrust generated by passive energy recapture was found to be dependent on the elastic properties of the jellyfish bell.

Key words: jellyfish, swimming, immersed boundary method, fluid-structure interaction, comparative biomechanics

1. Introduction

In many animals, locomotion emerges from the interplay of the active material properties of an organisms' musculature and the passive material properties of their flexible

† Email address for correspondence: ahoover2@tulane.edu

body or appendage. Elastic structures that bend and flex can be thought of as mechanical systems with their own natural frequency of vibration, or the frequency at which the system oscillates in free vibration. Since maximum deformations are generated when a flexible structure is driven at its natural frequency, it has been suggested that locomotory efficiency and performance is also maximized at this frequency (Alexander & Bennet-Clark 1977). The basis for this argument is that when an animal’s muscular processes are tuned to the elastic properties of their locomotory structures, the potential energy stored in the elastic structures during muscular deformation is maximized. The cessation of muscular activity in turn releases the stored potential energy and further drives the motion of the structure.

For swimming and flying animals, fluid motion also plays a significant role in determining the efficiency of locomotion. Independent and sometimes counter to the argument that performance is maximized when a structure is driven at its natural frequency, it is conjectured that locomotory performance is enhanced when the movement of the structure is tuned to nonlinear fluid effects, such as drag reduction (Ramanarivivo *et al.* 2011) or pressure-induced suction (Gemmell *et al.* 2015). On the other hand, resonant driving can enhance the transfer of momentum from the structure to the local fluid environment and lead to the formation strong vortex structures to drive the organism forward (Hoover *et al.* 2017*b*). Other arguments suggest that while resonance may play a large role with certain body shapes, other body shapes do not benefit due to effects of fluid damping (Tytell *et al.* 2010). The debate behind these two camps suggests the need for high fidelity models that incorporate both the nonlinear effects from the surrounding fluid environment and the elastic structures that account for the morphology and mechanical properties of the organism.

Jellyfish locomotion can be characterized as a process of active elastic deformation of a bell and passive recoil (Hoover & Miller 2015). The propulsive cycle of forward swimming jellyfish is initiated by the contraction of the coronal swimming muscles present in the subumbrellar cavity of the bell. This muscular contraction deforms the bell and pushes fluid out of the bell cavity, forming a starting vortex ring in the wake of the jellyfish. Following the cessation of muscular activity, the bell’s passive elastic properties, which are due to the mechanical properties of the mesoglea (Arai 1997), drive the expansion of the bell to its resting state. The expansion of the bell refills it with fluid. During this passive expansion, the motion of the bell margin forms a stopping vortex ring, which is rotating in the opposite direction of the starting vortex ring (Gemmell *et al.* 2014). The interaction between the starting and stopping vortex rings directs fluid from a region outside of the bell’s immediate wake upward into the bell cavity (Hoover *et al.* 2017*a*). This process, known as passive energy recapture (Gemmell *et al.* 2013), allows for a secondary source of thrust at no additional metabolic cost for the jellyfish. These vortex ring dynamics are particularly important for oblate jellyfish with a low fineness ratio where the stopping vortex ring continues to drive the bell forward and direct prey towards feeding structures. It has been suggested that these dynamics have allowed jellyfish to reach sizes that surpass the phylogenetic constraints of their musculature (Dabiri *et al.* 2005*a,b*, 2007).

A number of studies have considered jellyfish locomotion in the context of resonant driving. Demont & Gosline (1988) first noted the phenomena and used a reduced order lumped parameter model to characterize the bell as a spring-mass-damper system, with linear damping terms to describe the viscoelastic mesoglea and the shear of the surrounding fluid. Applying a sinusoidal force at the resonant frequency resulted in the 40% increase in the amplitude of the circumferential oscillation when compared to frequencies significantly above and below. Megill *et al.* (2005) further added to

the model by incorporating nonlinear spring elements that account for large strains. Recently, Hoover & Miller (2015) approached this problem numerically by solving the fully-coupled fluid-structure interaction problem. Using a 2-D elastic bell immersed in a viscous fluid, they found that driving near the resonant frequency produced a 50% increase in swimming speed relative to below the resonant frequency driving and even more gains when compared to frequencies significantly above the resonant frequency. There were several limitations of this model. The bell was driven using a sinusoidal driving force that actively re-expanded it, and the 2D model was only applied to the study of prolate bells, as the fluid dynamics of oblate bells are not well characterized in 2D (Herschlag & Miller 2011).

A number of other computational studies have examined the fluid dynamics behind jellyfish swimming (Huang & Sung 2009; Zhao *et al.* 2008). Sahin & Mohseni (2009) modeled the bell using an axisymmetric Lagrangian-Eulerian formulation to simulate the forward swimming of *Aequorea victoria* using recorded bell profiles. Herschlag & Miller (2011) tested Reynolds number effects using 2-D immersed boundary jellyfish models of oblate and prolate bells. Park *et al.* (2014) used a penalty immersed boundary method to drive the bell motion and explore wake structures. Alben *et al.* (2013) used a combination of computational tools and analytical models to quantify the kinematics of the bell for both high swimming and high efficiency movements. These studies did not specifically quantify the interplay between the bell’s material properties and passive energy recapture since the kinematics were prescribed or simplified.

Recently, Hoover *et al.* (2017a) developed a computational 3-D immersed boundary model of a forward swimming jellyfish whose kinematics are a consequence of the interaction between the bell’s material properties and the local fluid dynamics. In that study, the bell’s passive elastic and active muscular material properties were varied, and their effects on swimming performance were quantified. It was noted that the relative strength of the muscular contraction determined the strength and speed of advection of the vortex rings. However, this study did not examine the effects of passive energy recapture by varying the driving period.

In this study, we quantify the relationship between the driving frequency, the dynamics of passive energy recapture, and the resulting locomotory efficiency of jellyfish using the 3D numerical model described in Hoover *et al.* (2017a). First, we extract the period of free vibration for bells of differing material properties. We then drive the bell over a range of frequencies using a strength of muscular activation that is proportional to the effective stiffness of the bell. The frequencies are varied by fixing the duration of active contraction and varying the length of time the muscles are relaxed. The role of passive energy recapture is then quantified by measuring the strength of the stopping vortex ring. The performance of the bell at a given driving frequency is then quantified by examining the resulting swimming speed and input power. We then use swimming efficiency metrics, such as swimming economy and cost of transport, to compare the performance of bells with varying material properties.

2. Materials and methods

2.1. Fluid-structure interaction

Fluid-structure interaction problems are common to biological systems and have been examined with a variety of computational frameworks. The immersed boundary (IB) method (Mittal & Iaccarino 2005; Peskin 2002) is an approach to numerically solving fully-coupled fluid-structure interaction problems introduced by Peskin to study blood

flow in the heart (Peskin 1977). Since then, the IB method has been applied to a variety of fluid-structure interaction problems in biology in the low to intermediate Reynolds number regime, including undulatory swimming (Fauci & Peskin 1988; Bhalla *et al.* 2013; Hoover *et al.* 2017b), insect flight (Miller & Peskin 2004, 2005, 2009; Jones *et al.* 2015), lamprey swimming (Tytell *et al.* 2010, 2016), crustacean swimming (Zhang *et al.* 2014), and jellyfish swimming (Hamlet *et al.* 2011; Herschlag & Miller 2011; Hoover & Miller 2015; Hoover *et al.* 2017a).

The IB formulation of fluid-structure interaction uses an Eulerian description of the equations of fluid motion, and it uses a Lagrangian description of the elastic immersed boundaries. Let $\mathbf{x} = (x, y, z) \in \Omega$ denote physical Cartesian coordinates, with Ω denoting the physical region occupied by the fluid-structure system. Let $\mathbf{X} = (X, Y, Z) \in U$ denote Lagrangian material coordinates that describe the immersed structure, with U denoting the Lagrangian coordinate domain. The physical position of material point \mathbf{X} at time t is $\chi(\mathbf{X}, t) \in \Omega$, so that the physical region occupied by the structure at time t is $\chi(U, t) \subset \Omega$.

The immersed boundary formulation of the equations of motion is given by

$$\rho \left(\frac{\partial \mathbf{u}(\mathbf{x}, t)}{\partial t} + \mathbf{u}(\mathbf{x}, t) \cdot \nabla \mathbf{u}(\mathbf{x}, t) \right) = -\nabla p(\mathbf{x}, t) + \mu \nabla^2 \mathbf{u}(\mathbf{x}, t) + \mathbf{f}(\mathbf{x}, t) \quad (2.1)$$

$$\nabla \cdot \mathbf{u}(\mathbf{x}, t) = 0 \quad (2.2)$$

$$\mathbf{f}(\mathbf{x}, t) = \int_U \mathbf{F}(\mathbf{X}, t) \delta(\mathbf{x} - \chi(\mathbf{X}, t)) d\mathbf{X} \quad (2.3)$$

$$\int_U \mathbf{F}(\mathbf{X}, t) \cdot \mathbf{V}(\mathbf{X}) d\mathbf{X} = - \int_U \mathbb{P}(\mathbf{X}, t) : \nabla_{\mathbf{X}} \mathbf{V}(\mathbf{X}) d\mathbf{X} \quad (2.4)$$

$$\frac{\partial \chi(\mathbf{X}, t)}{\partial t} = \int_{\Omega} \mathbf{u}(\mathbf{x}, t) \delta(\mathbf{x} - \chi(\mathbf{X}, t)) d\mathbf{x} \quad (2.5)$$

in which ρ is the fluid density, μ is the dynamic viscosity, $\mathbf{u}(\mathbf{x}, t) = (u_x, u_y, u_z)$ is the Eulerian material velocity field, and $p(\mathbf{x}, t)$ is the Eulerian pressure field. Here, $\mathbf{f}(\mathbf{x}, t)$ and $\mathbf{F}(\mathbf{X}, t)$ are equivalent Eulerian and Lagrangian force densities. \mathbf{F} is defined in terms of the first Piola-Kirchhoff solid stress in Eq. 2.4 using a weak formulation, in which $\mathbf{V}(\mathbf{X})$ is an arbitrary Lagrangian test function. The Dirac delta function $\delta(\mathbf{x})$ appears as the kernel of the integral transforms, Eqs. 2.3 and 2.5, that connect the Eulerian and Lagrangian frames.

In this study, a hybrid finite difference/finite element version of the immersed boundary method (IB/FE) is used to approximate Eqs. 2.1-2.5. The IB/FE method uses a finite difference formulation for the Eulerian equations and a finite element formulation to describe the solid body. More details on the IB/FE method can be found in Griffith & Luo (2017).

2.2. Bell model and geometry

In the following subsection, we describe the structural model of the bell. In this study, the bell's motion is a result of the interaction between the passive elastic material properties of the bell, the active tension generated by the model of the coronal swimming musculature, and the interaction with the surrounding fluid. The structural stresses resulting from the bell's passive and active material properties are calculated using the first Piola-Kirchhoff stress tensor

$$\mathbb{P} = \mathbb{P}_p + \mathbb{P}_a, \quad (2.6)$$

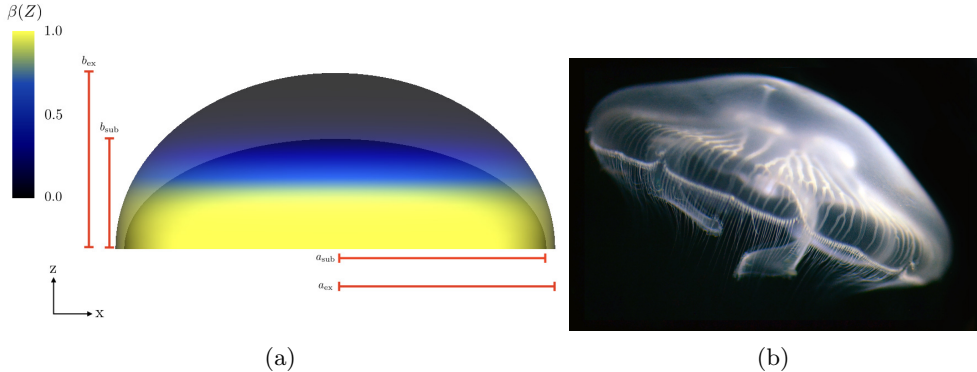


Figure 1: (a) A diagram of the bell model geometry with major and minor axes for the subumbrellar hemiellipsoid, a_{sub} and b_{sub} respectively, and the exumbrellar hemiellipsoid, a_{ex} and b_{ex} . Plotted on the bell is $\beta(Z)$, which describes the distribution of the subumbrellar musculature. (b) The model geometry draws inspiration from the oblate jellyfish, *Aurelia* spp.

Table 1: Table of dimensional parameters for the bell’s structural model. In this study the elastic modulus, η , and the maximum tension, T_{max} , are varied in proportion to one another and the values reported here are for the reference configuration.

Parameter	Symbol	Value
Elastic modulus	η_{ref}	75.0 Pa
Horizontal axis (exumbrellar)	a_{ex}	0.02 m
Horizontal axis (subumbrellar)	a_{sub}	0.019 m
Vertical axis (exumbrellar)	b_{ex}	0.016 m
Vertical axis (subumbrellar)	b_{sub}	0.01 m
Maximum tension	$T_{\text{max}}^{\text{ref}}$	75.0 N
Activation inflection point	Z_{lim}	0.0075 m
Musculature variable (spatial)	θ_s	700.0 m^{-1}
Musculature variable (activation)	θ_a	$200\pi \text{ sec}^{-1}$
Musculature variable (release)	θ_r	$200\pi \text{ sec}^{-1}$
Tension duration variable	t_{len}	0.3 sec

130 in which \mathbb{P}_p describes the passive elasticity of the body and \mathbb{P}_a describes the active tension generated by the muscle.

The passive elastic properties of the bell’s mesoglea are described using a neo-Hookean material model

$$\mathbb{P}_p = \eta(\mathbb{F} - \mathbb{F}^{-T}) \quad (2.7)$$

in which $\mathbb{F} = \frac{\partial \mathbf{x}}{\partial \mathbf{X}}$ is the deformation gradient and η is the elastic modulus of the material.

The contraction and release of the subumbrellar swimming muscles is modeled with time-dependent active stress on the bell. This circumferentially-oriented stress is applied over the lower portion of the bell, which is where the coronal swimming musculature is present. The active stress is calculated via

$$\mathbb{P}_a = J T \mathbb{F} \mathbf{f}_0 \mathbf{f}_0^T \quad (2.8)$$

in which $J = \det(\mathbb{F})$ is the Jacobian of \mathbb{F} , T is the magnitude of the prescribed tension, and \mathbf{f}_0 is the (fiber) direction vector of the prescribed tension with respect to the reference configuration. Here \mathbf{f}_0 is chosen to model the coronal orientation of the subumbrellar swimming musculature in the undeformed configuration.

The three-dimensional bell model developed for this study accounts for variations in the bell's thickness and material properties. Previous models (Daniel 1983; McHenry & Jed 2003; Herschlag & Miller 2011; Sahin *et al.* 2009) have described the bell geometry as a hemiellipsoid or by using functions fit to digitized bell shapes. In this study, the immersed body model is a hemi-ellipsoid bell with both exumbrellar and subumbrellar surfaces. The bell shape was parametrized using a hemiellipsoid description for the exumbrellar (ex) and subumbrellar (sub) surfaces via

$$\frac{(X - X_c)^2 + (Y - Y_c)^2}{a_{\text{ex,sub}}^2} + \frac{(Z - Z_c)^2}{b_{\text{ex,sub}}^2} = 1 \text{ for } Z \geq 0, \quad (2.9)$$

in which $\mathbf{X}_c = (X_c, Y_c, Z_c)$ is the center of the ellipsoid, $a_{\text{ex,sub}}$ is the radial axis of the subumbrellar and exumbrellar surfaces of the bell, respectively, and $b_{\text{ex,sub}}$ is its vertical axis (see Table 1 and Fig. 1). Variation in the bell thickness due to difference in the exumbrellar and subumbrellar dimensions accounts for variation in the elastic profile of the bell, where the thinner bell margin is more flexible than the thicker top of the bell. In all of the numerical studies reported here, as η is varied, T_{max} is also varied by the same proportion. This ensures the same amount of static deformation of the bell.

Below we describe how the active muscular tension is applied to the bell. The tension, T , applied at point \mathbf{X} varies in time and with respect to the height of the bell in its reference configuration, Z , and is given by

$$T = T_{\text{max}} \alpha(t) \beta(Z) \quad (2.10)$$

in which T_{max} is the maximum applied tension, $\alpha(t)$ is a temporal parametrization of the activation and release of muscular tension, and $\beta(Z)$ is a spatial parametrization of the distribution of the subumbrellar musculature. We remark that $0 \leq \alpha(t), \beta(Z) \leq 1$. A value of 0 implies either that no muscle is present or that the muscle is not activate.

Note that the subumbrellar musculature does not extend throughout the bell cavity, and tension is applied mainly at the margin of the bell. The region of activation is parameterized via

$$\beta(Z) = 1.0 - \frac{1}{1 + \exp(-\theta_s(Z - Z_{\text{lim}}))} \quad (2.11)$$

in which θ_s characterizes the transition from an area of active tension to an area where no tension is applied and Z_{lim} is the inflection point of the transition (see Fig. 1).

In this study, two sets of simulations are performed using different temporal patterns of activation described by $\alpha(t)$. The first set of simulations ends with free vibration of the bell. Active tension is initially applied in sustained manner before it is released to freely vibrate. In this case, $\alpha(t)$ is set to

$$\alpha(t) = \begin{cases} 1 & \text{for } t < 2 \\ 0 & \text{for } t \geq 2 \end{cases}. \quad (2.12)$$

In the second set of simulations that describe forward swimming, tension is repeatedly applied and released to induce a contraction of the bell's margin followed by a passive re-expansion of the bell. The function describing the activation of the muscle and the release of tension draws inspiration from the recordings of muscular contraction in *Aurelia*

Table 2: Table of dimensionless parameters and their nondimensionalizations.

Parameter	Symbol	Nondimensionalization
Time	\bar{t}	t/τ_{ref}^*
Cycle	\bar{t}^c	t/τ
Propulsive cycle period	$\bar{\tau}$	τ/τ_{ref}^*
Effective propulsive cycle period	$\bar{\tau}^*$	τ/τ^*
Vertical displacement	\bar{D}	D/L_{vert}
Elastic modulus	$\bar{\eta}$	$\eta/(\rho L^2 t_{\text{ref}}^{-2})$
Applied tensions	\bar{T}	$T/(\rho L^4 t_{\text{ref}}^{-2})$
Swimming Speed	\bar{V}	$V/(L_{\text{vert}}/\tau^*)$
Cycle swimming speed	\bar{V}^c	$V/(L_{\text{vert}}\tau^{-1})$
Inverse Strouhal number	St^{-1}	$V_{\text{avg}}/(L_{\text{rad}}\tau^{-1})$
Input power	\bar{P}	$TV_{\text{rad}}/(\rho L^4 t_{\text{ref}}^{-2} L_{\text{rad}}\tau^{-1})$

spp. found in the literature (Horridge 1954) and is parametrized via

$$\alpha(t) = \frac{1}{1 + \exp(-\theta_a t^*)} - \frac{1}{1 + \exp(-\theta_r(t^* - t_{\text{dur}})/\tau)} \quad (2.13)$$

$$t^* = \text{mod}(t, \tau) + t_0 \quad (2.14)$$

150 in which τ is the period of a swimming cycle, t_0 is an offset time for the initial function, θ_a characterizes the speed of muscular activation, θ_r characterizes the release of tension, and t_{dur} describes the duration of contraction. In the forward swimming study, t_{dur} is chosen such that the duration of active tension is held fixed as the period of the swimming cycle varies from 0.5 sec to 3.0 sec.

155 2.3. Dimensionless parameters

In this study, swimming performance is quantified using several dimensionless parameters (Table 2). The characteristic length of our system, L , corresponds to the diameter of the bell. A secondary length scale of L_{vert} , which correspond to the height of the bell, is also used to describe the forward swimming velocity. Note that in all simulations $L_{\text{vert}} = 0.4L$. The characteristic time, τ_{ref}^* , is given as the period of the initial free vibration of a bell with the characteristic elastic modulus ($\eta_{\text{ref}} = 75$ Pa). Note that this characteristic time is approximately 0.5 seconds. The vertical displacement of the bell, D , is nondimensionalized with respect to the bell height,

$$\bar{D} = \frac{D}{L_{\text{vert}}}, \quad (2.15)$$

while the radial displacement is nondimensionalized with respect to the bell radius,

$$\bar{D}_{\text{rad}} = \frac{D_{\text{rad}} - 0.5L}{0.5L}. \quad (2.16)$$

In the forward swimming study, the effective propulsive cycle period is defined as

$$\bar{\tau}^* = \tau/\tau^*, \quad (2.17)$$

where τ is the period of the propulsive cycle and τ^* is the period of free vibration for a bell of stiffness η . Here τ^* is found empirically from the free vibration study. Here $\bar{\tau}$ ranges from 1.0 to 6.0 for the reference case.

We introduce two other dimensionless temporal variables,

$$\bar{t} = t/\tau_{\text{ref}}^*, \quad (2.18)$$

and

$$\bar{t}^c = t/\tau, \quad (2.19)$$

where \bar{t} is nondimensionalized with respect to a fixed length of time and \bar{t}^c represent the point in time relative to the propulsive cycle. The reason for two temporal nondimensionalizations is that at times it is appropriate to examine the performance relative to the propulsive cycle, for which \bar{t}^c would be used, and other times it is appropriate to use a temporal variable that does not change with the driving frequency, for which \bar{t} would be used.

The elastic modulus, η , is nondimensionalized with respect to the characteristic elastic modulus,

$$\bar{\eta} = \frac{\eta}{\rho L^2 (\tau_{\text{ref}}^*)^{-2}}, \quad (2.20)$$

as is the applied tension, T ,

$$\bar{T} = \frac{T}{\rho L^4 (\tau_{\text{ref}}^*)^{-2}}. \quad (2.21)$$

For the reference configuration, $\bar{\eta}$ corresponds to 11.71875 and \bar{T} corresponds to roughly 7.32422×10^3 . In this study, \bar{T} is held proportional to $\bar{\eta}$.

The spatially averaged forward swimming speed, V , of the bell is recorded at each time step and non-dimensionalized using the equations

$$\bar{V} = \frac{V}{L_{\text{vert}}/\tau^*}, \quad (2.22)$$

where L_{vert} is the bell's height and τ^* is the period of free vibration. In this study, we report \bar{V}_{avg} , which is the average swimming velocity averaged over the length of the propulsive cycle, τ . Similarly, we calculate the cycle velocity, \bar{V}^c , here defined as

$$\bar{V}^c = \frac{V}{L_{\text{vert}}/\tau}, \quad (2.23)$$

where L_{rad} corresponds to the maximum radial displacement of the activated portion of the bell during the contraction phase of the swimming cycle. Here, \bar{V} and \bar{V}^c are two dimensionless swimming speeds with differing nondimensionalizations, where \bar{V} corresponds to a swimming speed relative to the free vibration period of the bell and \bar{V}^c corresponds to the speed relative to the period length of the propulsive cycle.

The cost of transport (COT), which is a measure of the energy spent per unit distance traveled, is quantified for each of the bell models. COT is often used as a measure of the efficiency of swimming (Bale *et al.* 2014; Schmidt-Nielsen 1972; Videler 1993). COT is defined by

$$COT = |\bar{\mathcal{E}}|/L_{\text{vert}}, \quad (2.24)$$

in which $\bar{\mathcal{E}}$ is the energy averaged over the propulsive cycle, and L_{top} is the vertical displacement of the top of the bell for the entire propulsive cycle. Here $\mathcal{E} = |D_{\text{rad}}|T$, where D_{rad} is the radial displacement of the margin, and T is the active tension and is normalized by the area of muscle activation. T and D_{rad} are spatially averaged over the margin of the bell, defined here as the region where $Z \leq Z_{\text{lim}}$ in the undeformed configuration.

Dimensionless power is also calculated as

$$\bar{P} = \bar{T} \frac{V_{\text{rad}}}{0.5L/\tau^*}, \quad (2.25)$$

where V_{rad} is the radial velocity of the bell margin. The swimming economy, which is the energy cost per unit of distance traveled, is defined as

$$\varepsilon = \frac{\bar{V}_{\text{avg}}}{\bar{P}_{\text{avg}}}, \quad (2.26)$$

where \bar{P}_{avg} is the input power averaged over the duration of the bell's swimming cycle.

The Reynolds number is a non-dimensional parameter that characterizes the ratio of inertial to viscous forces in the fluid. In this study, we report the Reynolds number using a frequency-based definition,

$$Re = \frac{\rho L (L_{\text{vert}} \tau^{-1})}{\mu} \quad (2.27)$$

where $L_{\text{vert}} \tau^{-1}$ is the characteristic velocity. We use a frequency based characteristic velocity rather than the resulting forward swimming speed so that Re is an input value known at the beginning of a simulation. See Table 2 for future reference.

The Eulerian variables have non-dimensional analogues for flow velocity

$$\bar{\mathbf{u}} = \frac{\mathbf{u}}{L/\tau^*} = (\bar{u}_x, \bar{u}_y, \bar{u}_z), \quad (2.28)$$

vorticity

$$\bar{\boldsymbol{\omega}} = \frac{\boldsymbol{\omega}}{1/\tau^*} = (\bar{\omega}_x, \bar{\omega}_y, \bar{\omega}_z), \quad (2.29)$$

and pressure

$$\bar{p} = \frac{p}{\rho L^2 (\tau^*)^2}. \quad (2.30)$$

We also report the magnitude of the dimensionless vorticity,

$$\bar{\omega}_{\text{mag}} = |\bar{\boldsymbol{\omega}}|, \quad (2.31)$$

and the radial velocity,

$$\bar{u}_{\text{rad}} = \text{sign}(y)(\bar{u}_x \cos(\theta) + \bar{u}_y \sin(\theta)), \quad \theta = \tan^{-1}(x/y), \quad (2.32)$$

which describes the fluid flow to and from the vertical axis.

2.4. Software implementation

The numerical model was implemented using IBAMR, a distributed-memory parallel implementation of the IB method that includes Cartesian grid adaptive mesh refinement (AMR) (IBAMR 2014). IBAMR relies on several open-source libraries, including SAMRAI (SAMRAI 2007; Hornung *et al.* 2006), PETSc (Balay *et al.* 2009, 1997), *hypre* (HYPRE 2011; Falgout & Yang 2002), and *libMesh* (Kirk *et al.* 2006). The computational domain was taken to be a cube of length $8L$ with periodic boundary conditions and was discretized using an adaptively refined grid for which the finest Cartesian grid spacing was $h = 8L/512$. The nondimensional time step was taken to be $\Delta t = 10^{-3}$. Note that the relative domain size with respect to the bell diameter is $8L \times 8L \times 8L$. The large domain size results in only minor interactions between the model jellyfish and the boundaries of the computational domain.

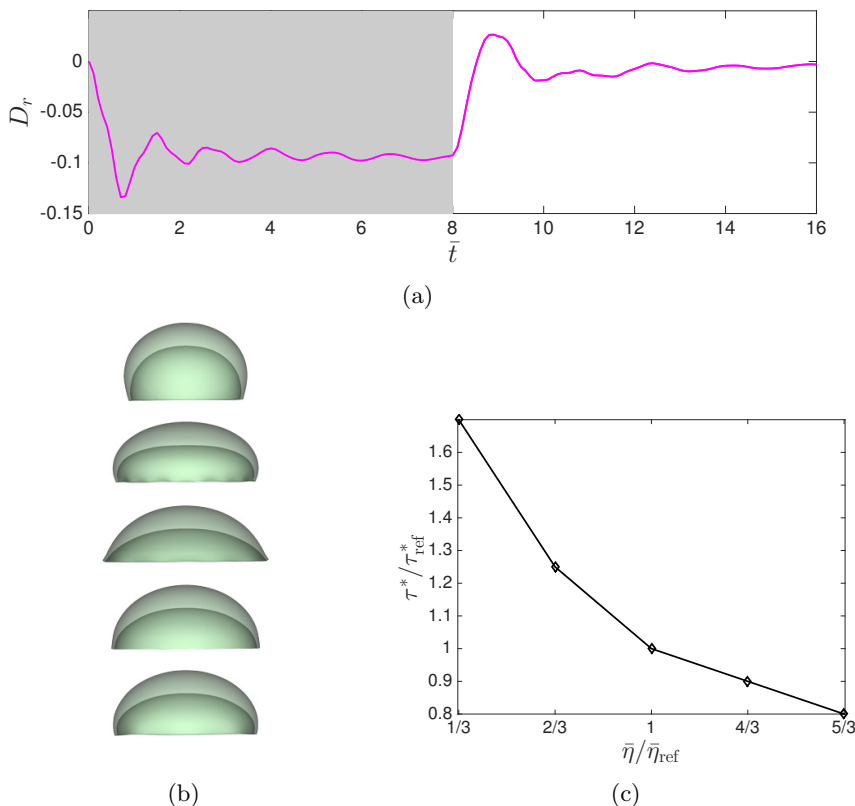


Figure 2: (a) Plot of the radial displacement, \bar{D}_r , during the free vibration study. Active tension is applied to the bell (in grey) and then released at $\bar{t} = 8.0$, allowing the bell's margin to oscillate at its frequency of free vibration. (b) Snapshots of the bell profile when tension is released from $\bar{t} = 8.0$ (top) to 10.0 at 0.5 intervals. (c) The recorded period of free vibration, τ^* , for different $\bar{\eta}$ relative to the reference case $\bar{\eta}_{\text{ref}}$.

3. Results

3.1. Free vibration study

To find the natural period free vibration, a coronally-oriented, constant tension is applied to the bell margin until the bell is deformed such that the passive elastic forces and active muscular tension are nearly in balance (Fig. 2a in grey). At $\bar{t} = 4.0$, the tension is then released and the passive elastic forces return the bell back to its resting configuration (Fig 2b). We then calculate the period of free vibration, $\bar{\tau}^*$, by measuring the time it took for the bell diameter to complete one oscillation as it expands and contracts back to its equilibrium configuration. For the reference configuration ($\bar{\eta} = \bar{\eta}_{\text{ref}}$), the period of free vibration was found to be $\bar{\tau}^* = 1.0$. Note that we estimate the natural frequency numerically rather than analytically since the effective mass of the jellyfish, due to the volume of the jellyfish and the boundary layer, is difficult to estimate at this Re for an unsteady object.

In this study, $\bar{\eta}$ is varied as the bell geometry is held fixed. To understand the relationship between $\bar{\eta}$ and $\bar{\tau}^*$, the free vibration simulations are run for different elastic moduli where $\bar{\eta} = \frac{1}{3}\bar{\eta}_{\text{ref}}$, $\frac{2}{3}\bar{\eta}_{\text{ref}}$, $\bar{\eta}_{\text{ref}}$, $\frac{4}{3}\bar{\eta}_{\text{ref}}$, and $\frac{5}{3}\bar{\eta}_{\text{ref}}$. Note that \bar{T} is held proportional to $\bar{\eta}$ throughout this study. This ensures similar deformations in the static case. We

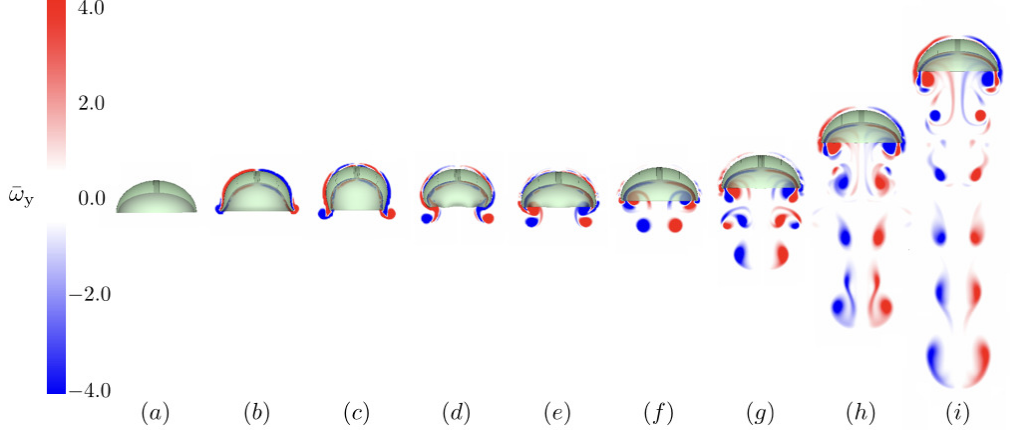


Figure 3: Out of plane vorticity ($\bar{\omega}_y$) for a bell with an elastic modulus of $\bar{\eta}_{\text{ref}}$ and period $\bar{\tau} = 2.0$ at $\bar{t} =$ (a) 0.0, (b) 0.125, (c) 0.25, (d) 0.625, (e) 0.75, (f) 1.0, (g) 2.0, (h) 4.0, and (i) 6.0.

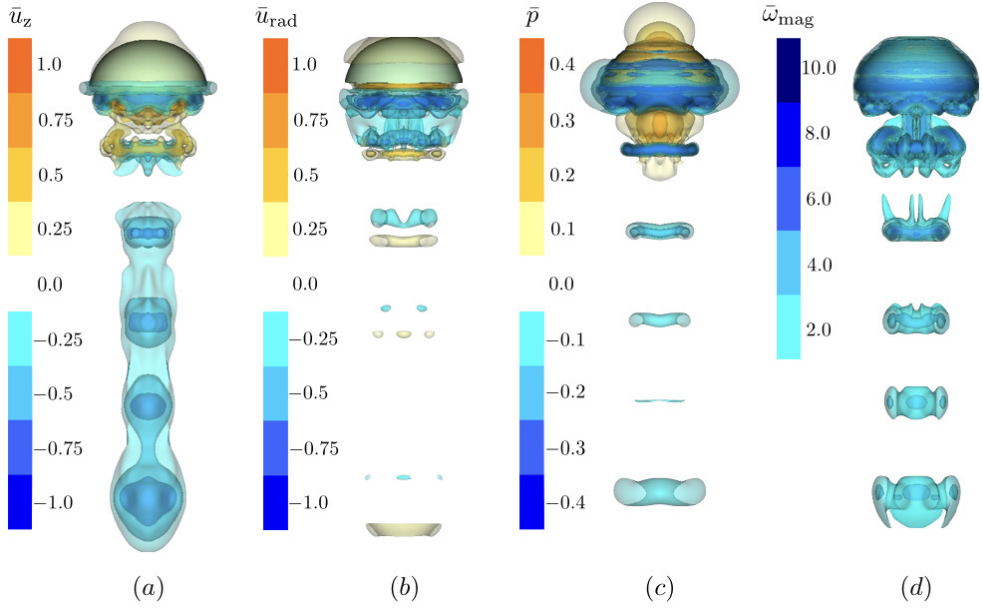


Figure 4: Plots of the isocontours of (a) $\bar{\omega}_{\text{mag}}$, (b) \bar{u}_z , (c) \bar{u}_{rad} , and (d) \bar{p} for a bell with an $\bar{\eta} = \bar{\eta}_{\text{ref}}$, $\bar{\tau} = 2.0$, and at $\bar{t} = 6.0$.

find that decreasing $\bar{\eta}$ increases the time it takes for the bell radius (r) to return to its resting configuration (r_0). We note that the resulting bell configurations during maximum contraction are similar because \bar{T} is held proportional to $\bar{\eta}$. Plotting the bell's period of free vibration as a function of the bell's stiffness (Fig. 2c), we find that $\bar{\tau}^*$ decreases as $\bar{\eta}$ increases.

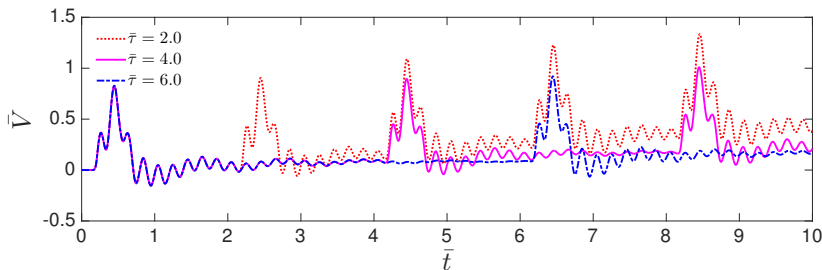


Figure 5: Plot of \bar{V} with respect to \bar{t} for three bells with $\bar{\tau} = 2.0, 4.0$, and 6.0 . The bell's elastic modulus is $\bar{\eta} = \bar{\eta}_{\text{ref}}$. Note that \bar{V} is the dimensionless velocity averaged over the entire bell. The duration of active contraction is fixed, while the rest period between active contractions is varied.

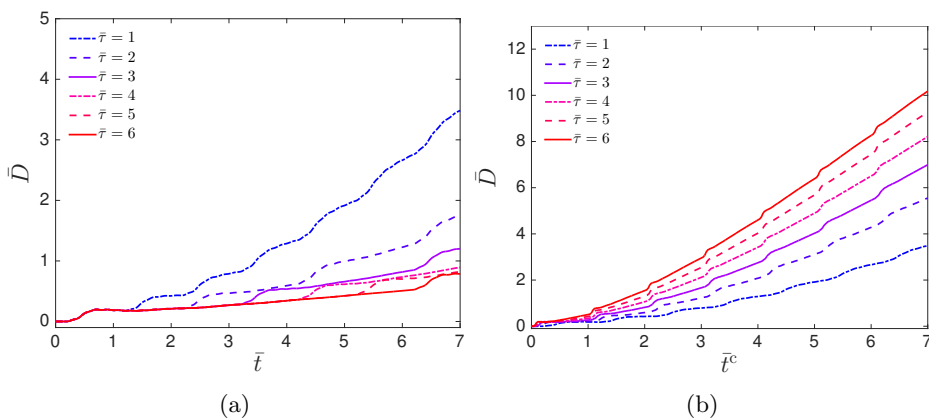


Figure 6: Plots of \bar{D} as a function of (a) time nondimensionalized by the base period of free vibration, \bar{t} , and (b) time nondimensionalized by the duration of the specific propulsive cycle for each case, \bar{t}^c , for bells with $\bar{\tau} = 1.0, 2.0, 3.0, 4.0, 5.0$, and 6.0 . Note that the bell driven at the natural frequency, $\bar{\tau} = 1$ travels the farthest for a fixed amount of time, while the bell with the longest pulsing period, $\bar{\tau} = 6$, travels the farthest per pulse.

3.2. Driving frequency study

To explore the interplay between the driving frequency and the role of passive energy recapture, the bell was driven over a range of frequencies, including the resonant frequency. The resulting swimming performance was then calculated using several metrics. The driving frequency was chosen by varying the period of the pulsing cycle, where $\bar{\tau} = 1.0$ through 6.0 in 0.25 increments. The total amount of tension applied on the bell margin over the course of the cycle was held fixed and the inter-pulse time was varied (e.g. the time between active contractions). The bells were driven for seven propulsive cycles, so as to measure their performance as they approach their steady state swimming speeds.

In Fig. 3, we show snapshots of the bell and the out-of-plane vorticity, $\bar{\omega}_y$, generated by the bell as it is driven with a propulsive cycle of length $\bar{\tau} = 2.0$. Initially at rest (Fig. 3a), the initiation of active muscular tension induces the contraction of the bell (Fig. 3b,c) and the resulting formation of the starting vortex ring in the wake of the bell. Once tension is released, the bell passively expands (Fig. 3d,e) to its resting configuration

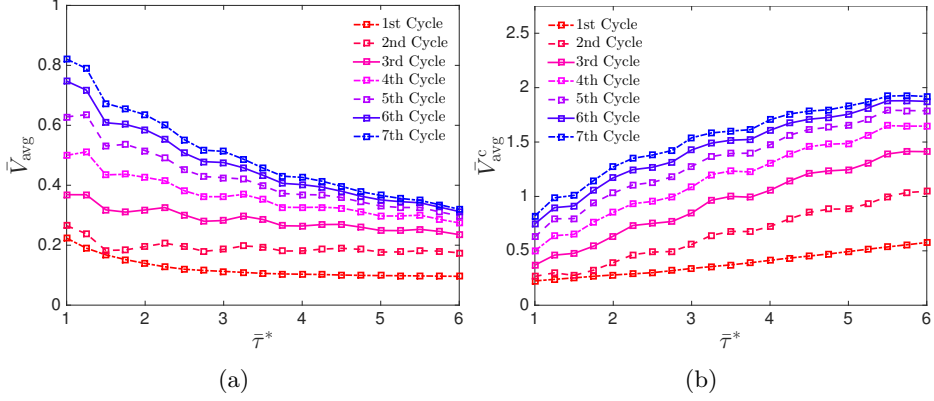


Figure 7: Plots of (a) the average dimensionless swimming speed, \bar{V}_{ave} and (b) the average dimensionless swimming speed determined by distance traveled per cycle, \bar{V}_{ave}^c as a function of $\bar{\tau}^*$. Average velocities are reported for each of the first seven propulsive cycles. With respect to absolute time, the fastest swimming speeds are obtained near the resonant driving frequency $\bar{\tau}^* = 1$. When the average velocity is calculated using the distance traveled per propulsive cycle, lower frequency bells swim farther.

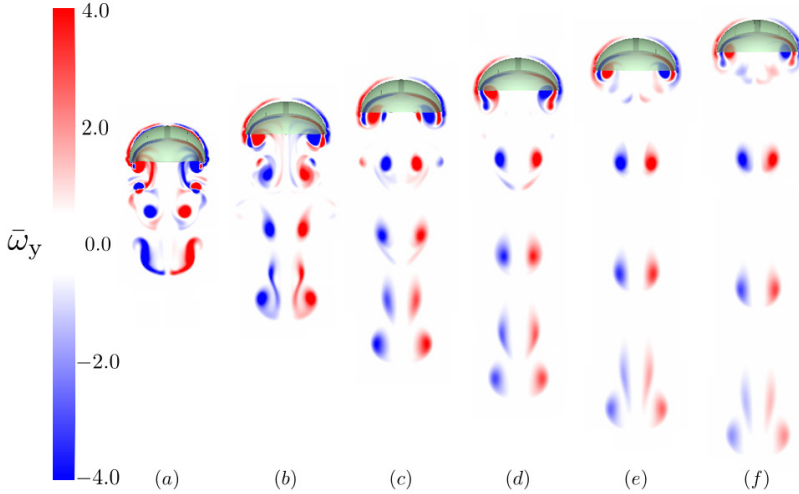


Figure 8: Plots of the out-of-plane vorticity, $\bar{\omega}_y$ at $\bar{t} = 4.0$ for bells with $\bar{\eta} = \bar{\eta}_{ref}$ and $\bar{\tau} =$ (a) 1.0, (b) 2.0, (c) 3.0, (d) 4.0, (e) 5.0, and (f) 6.0.

where the stopping vortex ring continues to drive the bell forward (Fig. 3f). Successive propulsive cycles (Fig. 3g-i) contribute more starting vortices to the wake, further driving fluid away from the bell while the stopping vortex continues to push the bell forward.

By examining the other Eulerian variables (Fig. 4) for a representative bell ($\bar{\tau} = 2.0$ at $t^c = 6.0$), the interaction between the starting and stopping vortex rings becomes more apparent. In Fig. 4a we plot isocontours of $\bar{\omega}_{mag}$. We note the presence of starting vortex rings in the wake of the bell, formed during the contraction phase of the previous propulsive cycles. The stopping vortex ring is visible near the subumbrellar cavity of the bell. The rotation of the starting vortex rings pull fluid away from the bell, leading to the formation of a long column of negative \bar{u}_z (Fig. 4b). Passive energy recapture effects

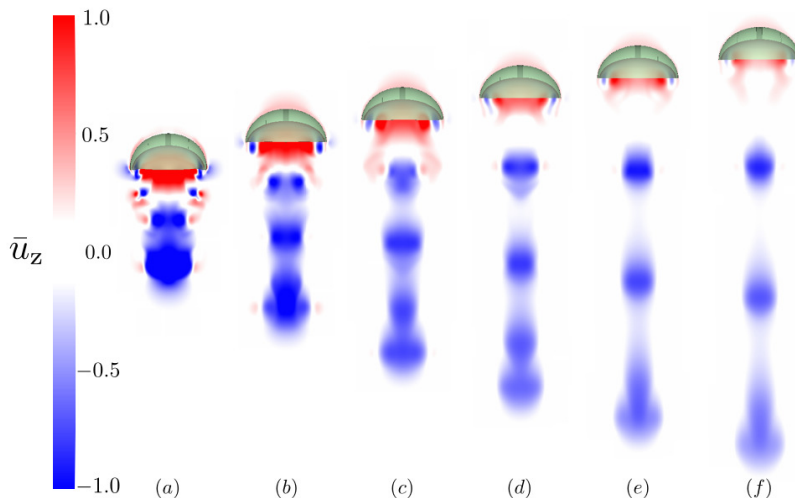


Figure 9: Plots of the vertical velocity, \bar{u}_z at $\bar{t} = 4.0$ for bells with $\bar{\eta} = \bar{\eta}_{\text{ref}}$ and $\bar{\tau} =$ (a) 1.0, (b) 2.0, (c) 3.0, (d) 4.0, (e) 5.0, and (f) 6.0.

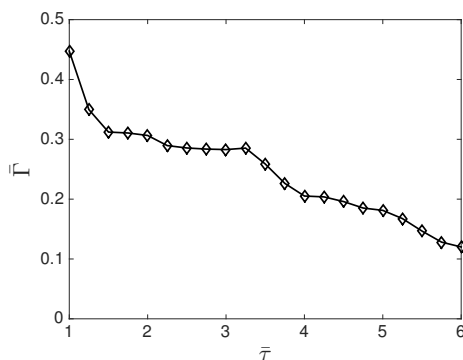


Figure 10: Plots of the stopping vortex ring circulation, $\bar{\Gamma}$, with respect to $\bar{\tau}$ at $\bar{t} = 7.0$ for a bell with $\bar{\eta} = \bar{\eta}_{\text{ref}}$.

can be seen with the interaction between the starting and stopping vortices, which rotate in opposite directions from one another, and produce positive \bar{u}_z in the wake near the subumbrellar cavity. Their interplay is also present when looking at \bar{u}_{rad} (Fig. 4c). In the immediate wake of the bell, a region of negative \bar{u}_{rad} indicates that the interaction between the starting and stopping vortex rings pulls the fluid toward the central axis of the bell in the immediate wake. This flow then causes a region of high \bar{p} (Fig. 4d) to form in the immediate wake.

In Fig. 5, we plotted \bar{V} with respect to \bar{t} for bells with $\bar{\tau} = 2.0, 4.0$, and 6.0 . Recall that the duration of applied active tension is held constant, and the length of time between active contraction is varied. Note that \bar{V} is averaged over the entire bell, which accounts for the observed high frequency oscillations in \bar{V} and are due to the bells' passive elastic properties. We note that the velocity profiles are identical in the initial contraction of the first propulsive cycle as the initial application of active tension is the same for all cases. When the second propulsive cycle for $\bar{\tau} = 2.0$ begins ($\bar{t} = 2.0$), the bell's velocity profile is the similar to the first propulsive cycle but slightly higher due to additional

fluid momentum generated during the first propulsive cycle. This profile is also observed in the second propulsive cycle of $\bar{\tau} = 4.0$ and 6.0 . We note the advantage of a lower $\bar{\tau}$ in accelerating the bell, where peak \bar{V} increases with each subsequent propulsive cycle.

The displacement of the top of the bell as a function of \bar{t} for different $\bar{\tau}$ is shown in Fig. 6a. We find that the initial profile of \bar{D} during the first propulsive cycle to be identical regardless of $\bar{\tau}$. This is due to how $\alpha(t)$ of Eq. (2.13) was chosen, where the strength of applied tension and the length of time it is held do not vary for differing τ . The bell quickly moves forward during the contraction phase of the bell, followed by the recoil of the expansion phase of the propulsive cycle. Following this expansion phase of the bell, we note that the bell continues to move forward long after the release of the active muscular tension, highlighting the role of stopping vortices in providing additional thrust during the passive energy recapture phase of the propulsive cycle. Comparing the displacement for different $\bar{\tau}$, we note that bells with a shorter $\bar{\tau}$ accelerate more quickly than those with a longer τ . Plotting \bar{D} with respect to time nondimensionalized by the specific the pulse period, \bar{t}^c (Fig. 6b), we find that bells with a longer $\bar{\tau}$ swim farther over the total length of their cycle.

Driving the bell near the resonant frequency ($\bar{\tau}^* = 1$) yielded higher swimming speeds over the propulsive cycle. In Fig. 7a, we show \bar{V}_{avg} as a function of $\bar{\tau}$ over the seven propulsive cycles. We note that the optimal driving frequency is at the resonant frequency ($\bar{\tau} = 1.0$). Examining the performance of the bell for lower frequencies, we note that the peak \bar{V}_{avg} shifts from a $\bar{\tau}$ that is slightly longer than $\bar{\tau}^*$ during the intermediate cycles before shifting to $\bar{\tau}^*$. This is possibly due to added mass effects that shift as the the swimming speed increases and the boundary layer of the bell decreases. We also note the presence of a second, lower peak in \bar{V} near $\bar{\tau} = 2.25$ in the intermediate cycles. In later cycles, this second peak shifts to $\bar{\tau} = 2.0$ and 1.75 .

Bells with longer periods traveled farther per propulsive cycle than those with shorter periods. Plotting \bar{V}_{avg}^c with respect to $\bar{\tau}$ (Fig. 7b), we generally find that \bar{V}_{avg}^c increases as $\bar{\tau}$ increases, with \bar{V}_{avg}^c plateauing for $\bar{\tau} \geq 5.5$ at later cycles. Recall that \bar{V}_{avg}^c describes the bell heights traveled per propulsive cycle. This illustrates the role of the stopping vortex ring in generating forward movement after the expansion phase. As the $\bar{\tau}^*$ increases, the passive energy recapture due to the stopping vortex ring continues to propel the bell forward for no additional energy cost. For $t\bar{a}u \geq 5.5$, the additional distance traveled due to the stopping vortex ring does not increase relative to the distance traveled for bells with shorter periods.

As the period of the propulsive cycle increases, the distance between the starting and stopping vortex rings increases as well. In Fig. 13, we plot $\bar{\omega}_y$ at $\bar{t} = 4.0$ for bells with $\bar{\tau} = 1.0, 2.0, 3.0, 4.0, 5.0$ and 6.0 . For all cases considered, starting vortex rings are shed into the the wake of the bell, and stopping vortices are observed in the subumbrellar cavity. As $\bar{\tau}$ increases, the distance between the stopping and starting vortex ring increases, as does the distance between starting vortex rings from previous propulsive cycles. To illustrate these difference in the wake we plot the instantaneous vertical flow, \bar{u}_z , in the xz -plane. As the distance between the starting and stopping vortex ring increases, the strength of their interaction decreases, with a smaller region of positive vertical velocity present in the immediate wake. The immediate wake of the bell with $\bar{\tau} = 1.0$ is also affected by the starting vortex ring in the third propulsive cycle.

To quantify the strength of the stopping vortex ring, its dimensionless circulation, $(\bar{\Gamma})$, was calculated at the end of the bells' seventh propulsive cycle. In Fig. 10, we show $\bar{\Gamma}$ as a function of $\bar{\tau}$. An initial peak in circulation is present at $\bar{\tau} = 1.0$, which is followed by a steep decline to a plateau where the circulation remains nearly constant from $\bar{\tau} = 1.5$

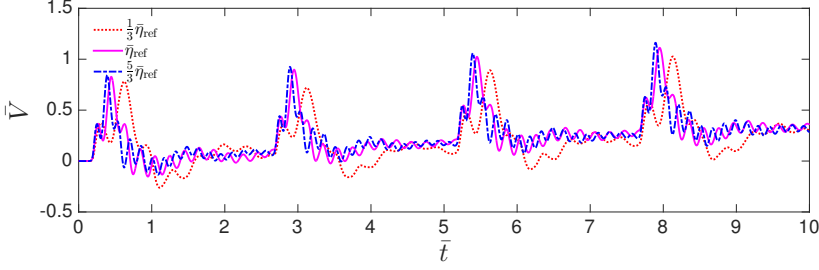


Figure 11: Plot of \bar{V} with respect to \bar{t} for three bells with $\bar{\eta} = \frac{1}{3}\bar{\eta}_{\text{ref}}$, $\bar{\eta}_{\text{ref}}$, and $\frac{5}{3}\bar{\eta}_{\text{ref}}$. The bell's propulsive cycle has a period of $\bar{\tau} = 2.5$. Note that \bar{V} is the dimensionless velocity averaged over the entire bell.

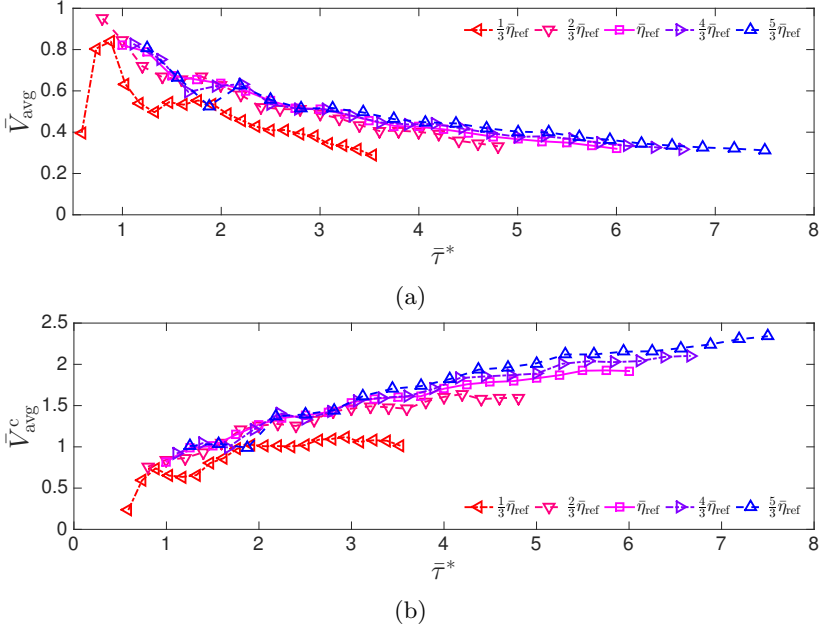


Figure 12: Plot of (a) \bar{V}_{avg} and (b) \bar{V}_{avg}^c with respect to $\bar{\tau}^*$ for bells with $\bar{\eta} = \frac{1}{3}\bar{\eta}_{\text{ref}}$, $\bar{\eta}_{\text{ref}}$, and $\frac{5}{3}\bar{\eta}_{\text{ref}}$. Note that $\bar{\tau}^* = 1$ corresponds to the natural frequency of each of the bells. \bar{V}_{avg} denotes the dimensionless swimming speed with respect to absolute time. \bar{V}_{avg}^c denotes the average dimensionless swimming speed calculated using distance traveled per propulsive cycle. Hence, (b) shows that bells with longer driving periods swim farther per propulsive cycle.

to 3.25. After this point, the circulation decreases at a higher rate. This suggests that there is a limit to the additional thrust generated by the stopping vortex rings due to viscous dissipation.

310 3.2.1. Varying bell stiffness

To further examine the role of resonance, we varied the bell's elastic modulus (see Table 1) and varied the driving frequency. In Fig. 11, we plotted \bar{V} with respect to \bar{t} for three bells of with elastic moduli of $\frac{1}{3}\bar{\eta}_{\text{ref}}$, $\bar{\eta}_{\text{ref}}$ and $\frac{5}{3}\bar{\eta}_{\text{ref}}$, and a propulsive cycle of length $\bar{\tau} = 2.5$. We remind that \bar{V} is nondimensionalized with respect to the bell's period of free

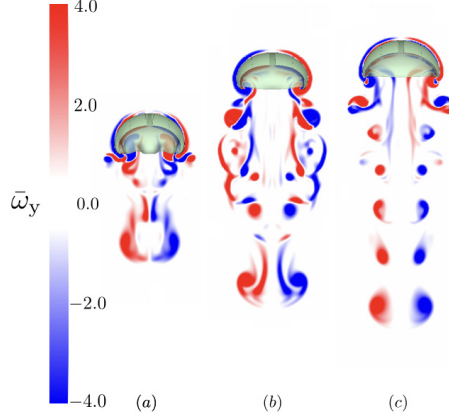


Figure 13: Plot of $\bar{\omega}_y$ for bells with $\bar{\tau} = 0.5$ at $\bar{t} = 7.0$ for $\bar{\eta}$ equal to (a) $\frac{1}{3}\bar{\eta}_{\text{ref}}$, (b) $\frac{2}{3}\bar{\eta}_{\text{ref}}$, and (c) $\bar{\eta}_{\text{ref}}$. The bell in (a) has not fully expanded at the end of its propulsive cycle, and does not form the defined starting vortex rings as found in the wakes of (b) and (c). The bell in (a) lacks the large region of positive \bar{u} found in (b) and (c). Note that the bell in (a) is driven faster than its resonant frequency, while the bell in (c) is being driven at its resonant frequency. The bell in (b) is being slightly faster than its resonant frequency ($\bar{\tau}^* = 0.8$) but is allowed enough time to expand.

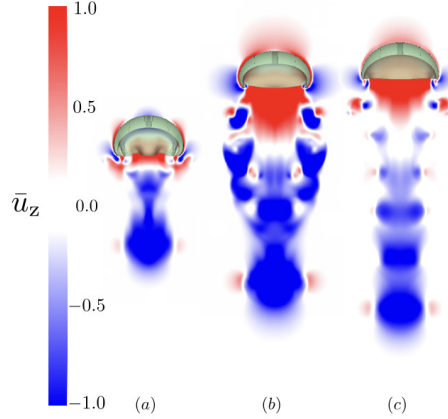


Figure 14: Plot of \bar{u}_z on the xz -plane for bells with $\bar{\tau} = 0.5$ at $\bar{t} = 7.0$ for $\bar{\eta}$ equal to (a) $\frac{1}{3}\bar{\eta}_{\text{ref}}$, (b) $\frac{2}{3}\bar{\eta}_{\text{ref}}$, (c) $\bar{\eta}_{\text{ref}}$. The bell in (a) lacks the large region of positive \bar{u} found in (b) and (c). Note that the bell in (a) is driven faster than its resonant frequency, while the bell in (c) is being driven at its resonant frequency. The bell in (b) is being slightly faster than its resonant frequency ($\bar{\tau}^* = 0.8$) but still performs well.

315 vibration, τ^* , and that it is averaged over the entire bell. We find that \bar{V} for all three
 bells display oscillations in the forward swimming speed, as seen in Fig. 5, but that the
 frequency of those oscillations varies as a function of $\bar{\eta}$, with higher frequency oscillations
 occurring for the stiffest bell ($\frac{5}{3}\bar{\eta}_{\text{ref}}$) and lower frequency oscillations for the most flexible
 bell ($\frac{1}{3}\bar{\eta}_{\text{ref}}$). We also note that the point at which peak \bar{V} occurs shifts to later in the
 320 propulsive cycle as $\bar{\eta}$ decreases.

Plotting \bar{V}_{avg} of the seventh propulsive cycle with respect to the effective period, $\bar{\tau}^*$,

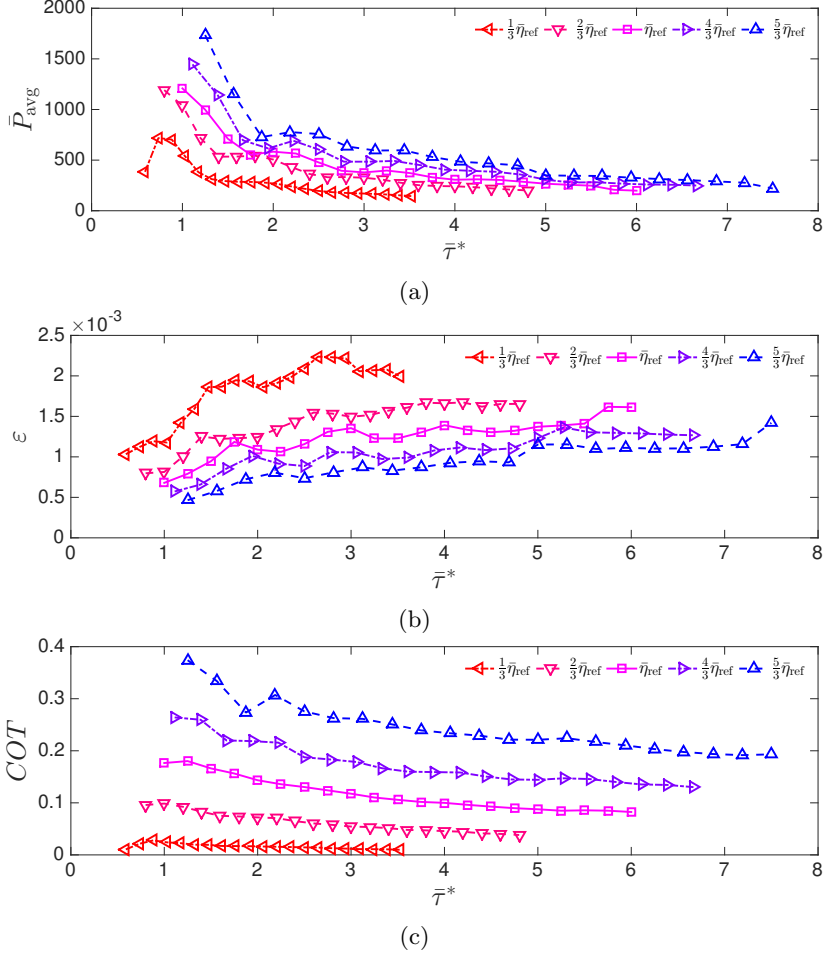


Figure 15: Plot of (a) average inputted power (\bar{P}_{avg}), (b) swimming economy (ε), and (c) cost of transport (COT) with respect to $\bar{\tau}^*$ for bells with $\bar{\eta} = \frac{1}{3}\bar{\eta}_{ref}$, $\bar{\eta}_{ref}$, and $\frac{5}{3}\bar{\eta}_{ref}$. Recall that the bells are driven at their resonant frequency when $\bar{\tau}^* = 1$.

we find that the bell swims fastest when the propulsive cycle is equal to its period of free vibration ($\bar{\tau}^* = 1.0$) or slightly less than it. If the period is too short, as seen for the first point of the $\frac{1}{3}\bar{\eta}_{ref}$ curve, the bell does not produce significant forward swimming speed. For $\bar{\tau}^* > 1.0$ we see a steady decline in \bar{V}_{avg} , as previously observed in Fig. 7b. Examining \bar{V}_{avg}^c in Fig. 12b, we find that longer $\bar{\tau}^*$ travel farther per cycle, but \bar{V}_{avg}^c levels off at earlier $\bar{\tau}^*$ when $\bar{\eta}$ is lower.

To further examine the role of resonance, we show the our of plane vorticity, $\bar{\omega}_y$, for three bells with the elastic modulus set to $\frac{1}{3}\bar{\eta}_{ref}$, $\frac{2}{3}\bar{\eta}_{ref}$ and $\bar{\eta}_{ref}$ driven with a propulsive cycle period of $\bar{\tau} = 1.0$ (Fig. 13). The most flexible case ($\frac{1}{3}\bar{\eta}_{ref}$) is driven above its resonant frequency, and is not given enough time during the propulsive cycle to expand fully to its resting state. As such the bell is not fully expanded by the time the next propulsive cycle begin, leading to a less defined starting vortex ring. We find that the distinct separation of the starting vortex rings in the wake, as seen in the higher $\bar{\eta}$ cases, is absent. Also absent for the more flexible bell is the separation of the starting and stopping vortex rings in the immediate wake. Examining the vertical velocity in a 2D plane through the

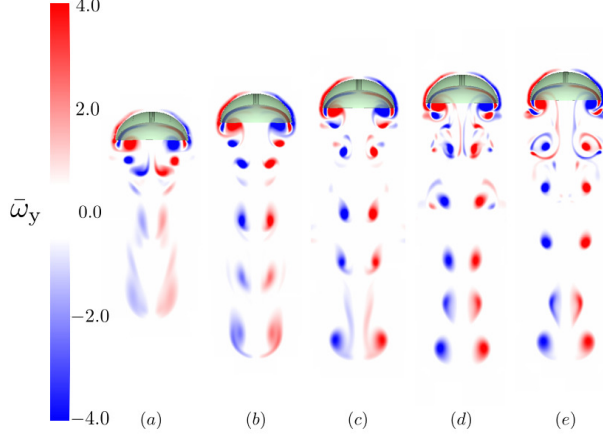


Figure 16: Plot of $\bar{\omega}_y$ for bells with $\bar{\tau} = .5$ at $\bar{t} = 6.0$ for $\bar{\eta}$ equal to (a) $\frac{1}{3}\bar{\eta}_{\text{ref}}$ ($\bar{\tau} = 4.25$), (b) $\frac{1}{3}\bar{\eta}_{\text{ref}}$ ($\bar{\tau} = 3.0$), and (c) $\bar{\eta}_{\text{ref}}$ ($\bar{\tau} = 2.5$), (d) $\frac{4}{3}\bar{\eta}_{\text{ref}}$ ($\bar{\tau} = 2.25$), and (e) $\frac{5}{3}\bar{\eta}_{\text{ref}}$ ($\bar{\tau} = 2.0$).

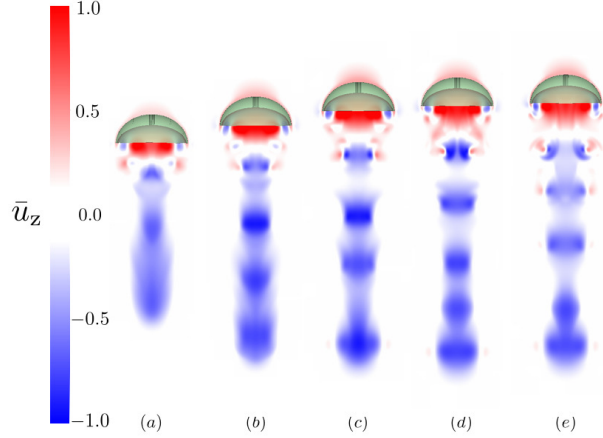


Figure 17: Plot of \bar{u}_z on the xz -plane for bells with $\bar{\tau}^* \approx 2.5$ at $\bar{t} = 6.0$ for $\bar{\eta}$ equal to (a) $\frac{1}{3}\bar{\eta}_{\text{ref}}$ ($\bar{\tau} = 4.25$), (b) $\frac{1}{3}\bar{\eta}_{\text{ref}}$ ($\bar{\tau} = 3.0$), (c) $\bar{\eta}_{\text{ref}}$ ($\bar{\tau} = 2.5$), (d) $\frac{4}{3}\bar{\eta}_{\text{ref}}$ ($\bar{\tau} = 2.25$), and (e) $\frac{5}{3}\bar{\eta}_{\text{ref}}$ ($\bar{\tau} = 2.0$).

central axis of the bell (Fig. 14), we find that the absence of this vortex ring separation yields a smaller region of positive \bar{u}_z in the immediate wake. A video detailing this case has been included in the supplementary materials.

To describe the efficiency as a function of the bell elastic modulus and the driving frequency, we calculated that average power input, \bar{P}_{avg} , the swimming economy, ϵ , and the cost of transport, COT, for each of the cases. \bar{P}_{avg} generally decreased as the effective period, $\bar{\tau}^*$, increased (Fig. 15a). When the bell was driven above its natural frequency, $\bar{\tau}^* < 1.0$ for $\frac{1}{3}\bar{\tau}$, the average power input was lower since less work was done as the bell did not fully expand. There was a second local peak in \bar{P}_{avg} at $\bar{\tau}^* \approx 2.25$ for all $\bar{\eta}$. For fixed $\bar{\tau}^*$, \bar{P}_{avg} was higher for stiffer bells, due to this study maintaining tension magnitude in proportion to the bell's elastic modulus. Examining the swimming economy of the bell, ϵ , with respect to the effective period, $\bar{\tau}^*$, we found that the swimming economy increased as bell stiffness decreased (Fig. 15b). Local minima were noted at $\bar{\tau}^*$ that correspond to

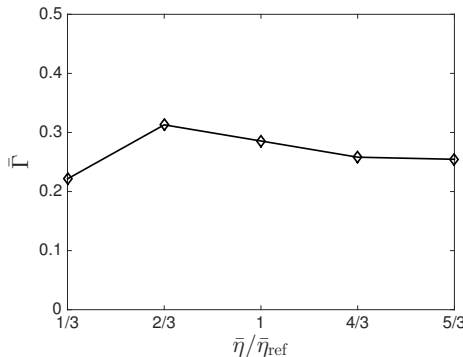


Figure 18: Plot of the dimensionless stopping vortex ring circulation, $\bar{\Gamma}$, vs the normalized elastic modulus of the bell, $\bar{\eta}/\bar{\eta}_{ref}$, for five bells with $\bar{\tau}^* \approx 2.5$ at $\bar{t} = 7.0$.

where local peaks in power input occur. Similarly, more flexible bells had a lower cost of transport, COT . Increasing the pulsing cycle duration, $\bar{\tau}$, led to a decrease in COT for a given stiffness (Fig. 15c).

Collapsing our results with respect to $\bar{\tau}^*$ allowed us to compare bells of different stiffnesses relative to the period of free vibration. We generally find that bells driven at the same $\bar{\tau}^*$ have similar \bar{V}_{avg} and \bar{V}_{avg}^c , with the exception being the most flexible case, $\frac{1}{3}\bar{\eta}_{ref}$, which swims at a slightly slower speed. Plotting the vorticity associated with bells of $\bar{\tau}^* \approx 2.5$ (Fig. 16), we find similarity in the vorticity profiles of the bells. Note that the bells are driven at different frequencies. Plotting \bar{u}_z on the xz -plane for the bells reveal similarities in the immediate wake of the bell. In that region, positive \bar{u}_z is present due to the starting and stopping vortex ring interactions (Fig. 17). Calculating the dimensionless circulation at $\bar{t} = 7.0$ for the five bells of Fig. 16 and 17, we find that the circulation of the stopping vortex ring remains fairly consistent across the five bells of varying $\bar{\eta}$ and $\bar{\tau}$. A video detailing this case has been included in the supplementary materials.

4. Discussion

Our three-dimensional numerical study of resonant driving and passive energy recapture in oblate jellyfish bells indicates that the ideal driving frequency for a given bell depends upon the metric that is to be optimized. For a given bell shape and elastic modulus with a fixed magnitude and duration of applied muscular tension, the fastest forward swimming speeds are generated when the bell is driven near its resonant frequency. If the bell is driven above this frequency, it will not fully expand before the next active contraction. This results in lower amplitude oscillations and weaker starting and stopping vortex rings that are not efficiently shed into the wake. If the bell is driven below this frequency, the average distance traveled per unit time decreases, due in part to the fact that the contractions happen less frequently. On the other hand, long coasting periods between active contractions (corresponding to lower driving frequencies) result in more efficient swimming when one considers the cost of transport and average power input. The bell is passively propelled forward for longer periods of time due to its interaction with the stopping vortex ring, though there are limits to this secondary thrust mechanism due to viscous dissipation of the stopping vortex ring.

Our results complement but also expand our understanding of resonant swimming in jellyfish relative to previous work. The lumped parameter models by Demont & Gosline

(1988) and Megill (2002) showed that the fastest forward swimming speeds are obtained when the bell is driven at its resonant frequency. These works did not, however, show that lower frequencies lead to more efficient swimming as the models did not consider unsteady effects of the fluid or vortex-bell interactions. Hoover & Miller (2015) found that for two-dimensional prolate bells, both swimming speed and cost of transport were maximized when the bell was driven near its resonant frequency. Given the prolate bell geometry and the two-dimensionality of the simulations, passive energy recapture did not have a significant effect. In our three-dimensional simulations of oblate bells, the jellyfish can coast for extended periods of time through passive energy recapture. While the average swimming speeds are slower, efficiency of movement is higher. Other differences between our results and previous models may also be due to the way in which muscular forces are applied. In earlier resonant studies, these forces are given as sinusoidal functions such that the duration of applied tension changes with driving frequency. There is also an active force during expansion that acts to re-expand the bell. By keeping the duration of applied tension constant in our model and applying no force to re-expand the bell, we note that our model of muscular tension is more representative of true jellyfish.

This study also further illuminates the role of passive energy recapture in jellyfish locomotion. A recent experimental study by Gemmell *et al.* (2017) observed that though passive energy recapture occurs throughout the jellyfish taxa, not all jellyfish take full advantage of this mechanism. In that study it was remarked that one possible reason for this discrepancy is that jellyfish that are continuously swimming want to avoid the loss of inertia associated with longer inter-pulse durations. The results from our study confirm this observation, with significantly lower \bar{V}_{avg} for the reference bell with long $\bar{\tau}$ (Fig. 7a) and diminishing returns for the distance traveled by a bell over the propulsive cycle (Fig. 7b). We note that the resulting steady-state or near-steady state swimming is higher for bells with shorter $\bar{\tau}$ for the reference case. Furthermore, examining the circulation of the stopping vortex (Fig. 10) at the end of the propulsive cycle revealed a steady decline in circulation for $\bar{\tau} \geq 3.5$. This suggests that, after this point, there are diminishing returns on the additional thrust from passive energy recapture due to the decline of the intensity of the stopping vortex ring.

Comparing the swimming performance of bells with differing material properties (Figs. 12a and 12b) further reveals the dynamics between passive energy recapture and resonant driving. Bells driven near $\bar{\tau}^* = 1.0$ have a higher \bar{V}_{avg} than bells driven with a long $\bar{\tau}^*$. Bells with a longer $\bar{\tau}^*$ in turn travel farther per propulsive cycle and therefore have a higher \bar{V}_{avg}^c . The two most flexible bells, $\frac{1}{3}\eta_{\text{ref}}$ and $\frac{1}{3}\eta_{\text{ref}}$, are driven at $\bar{\tau}^* < 1$ and reveal the dynamics of the driving the bell above its resonant frequency. Driving slightly above the resonant frequency can yield faster swimming speeds than driving at the resonant frequency, but if the frequency is too high (Figs. 13 and 13) the bell does not fully expand and does not fully form the starting and stopping vortex rings present in jellyfish locomotion. To further characterize the swimming performance, we examined the efficiency of the bell by examining the swimming economy, ε , and cost of transport, COT , of the bell. We generally found a higher swimming economy for more flexible bells (Fig. 15b) and for bells that are driven at longer $\bar{\tau}^*$. We note that the swimming economy revealed that a flexible bell driven with a shorter $\bar{\tau}^*$ would have the equivalent swimming economy as a stiff bell driven with a longer $\bar{\tau}^*$. Examining cost of transport (Fig. 15c) we generally find that flexible bells have a lower cost of transport. Driving at the resonant frequency led to a higher average input power, \bar{P}_{avg} , which can explain the lower efficiency associated with $\bar{\tau} \approx 1$.

The collapse of \bar{V}_{avg} for bells of differing material properties using $\bar{\tau}^*$ also reveals the interplay between the material properties of the structure and the fluid motion it

generates. Using the period of free vibration, τ^* , as the characteristic time for \bar{V} , we find that for bells with $\bar{\eta} \geq \frac{2}{3}\bar{\eta}_{\text{ref}}$ the resulting swimming performance is dependent on the speed of the bell's expansion. Stiffer bells have a lower τ^* and the bell will expand more quickly to its resting configuration. During this expansion, the strength of the stopping vortex ring formed will be dependent on the speed of expansion, with a higher transfer of momentum for lower τ^* . Since passive energy recapture is dependent on the strength of the stopping vortex, scaling $\bar{\tau}^*$ with τ^* , we find that bells of similar $\bar{\tau}^*$ have a similar velocity and displacement, even with differences in the driving frequency (Figs. 16 and 17). This further elucidates the relationship between the bell's material properties and the fluid forces the bell generates. This relationship was also examined in Hoover *et al.* (2017a), where the speed of the starting vortex rings was found to be dependent on the strength of the applied active tension. However, the length of the propulsive cycle was held fixed in that study and the effects that the material properties have on passive energy recapture were not fully examined. The results from our study further explain how these material properties affect the strength of the starting and stopping vortex rings and their role in both resonant driving and passive energy recapture.

5. Acknowledgements

We would like to thank Ricardo Cortez, Lisa Fauci, and Boyce Griffith for their advice and insights throughout this research project. This research was funded by a National Science Foundation (NSF) DMS CAREER no. 1151478 (to L.A.M.). A.J.P. was supported with the University of North Carolina at Chapel Hill's Summer Undergraduate Research Fellowship. We also thank Grace McLaughlin, who took the *Aurelia* spp. photo in Fig. 1. All other images were generated in Matlab and VisIt.

REFERENCES

- ALBEN, SILAS, MILLER, LA & PENG, JIFENG 2013 Efficient kinematics for jet-propelled swimming. *Journal of Fluid Mechanics* **733**, 100–133.
- ALEXANDER, R MCN & BENNET-CLARK, HC 1977 Storage of elastic strain energy in muscle and other tissues. *Nature* **265** (5590), 114–117.
- ARAI, MARY N 1997 *A functional biology of Scyphozoa*. Springer Science & Business Media.
- BALAY, S, ABHYANKAR, S, ADAMS, M, BROWN, J, BRUNE, P, BUSCHELMAN, K, ELJKHOUT, V, GROPP, W, KAUSHIK, D, KNEPLEY, M & OTHERS 2009 PETSc: Web page. <http://www.mcs.anl.gov/petsc>.
- BALAY, SATISH, GROPP, WILLIAM D, MCINNES, LOIS CURFMAN & SMITH, BARRY F 1997 Efficient management of parallelism in object-oriented numerical software libraries. In *Modern software tools for scientific computing*, pp. 163–202. Springer.
- BALE, RAHUL, HAO, MAX, BHALLA, AMNEET PAL SINGH & PATANKAR, NEELESH A 2014 Energy efficiency and allometry of movement of swimming and flying animals. *Proceedings of the National Academy of Sciences* **111** (21), 7517–7521.
- BHALLA, AMNEET PAL SINGH, BALE, RAHUL, GRIFFITH, BOYCE E & PATANKAR, NEELESH A 2013 A unified mathematical framework and an adaptive numerical method for fluid–structure interaction with rigid, deforming, and elastic bodies. *Journal of Computational Physics* **250**, 446–476.
- DABIRI, JOHN O, COLIN, SEAN P & COSTELLO, JOHN H 2007 Morphological diversity of medusan lineages constrained by animal–fluid interactions. *Journal of Experimental Biology* **210** (11), 1868–1873.
- DABIRI, JOHN O, COLIN, SEAN P, COSTELLO, JOHN H & GHARIB, MORTEZA 2005a Flow patterns generated by oblate medusan jellyfish: field measurements and laboratory analyses. *The Journal of Experimental Biology* **208** (7), 1257–1265.
- DABIRI, JOHN O, GHARIB, MORTEZA, COLIN, SEAN P & COSTELLO, JOHN H 2005b Vortex

motion in the ocean: in situ visualization of jellyfish swimming and feeding flows. *Physics of Fluids* **17** (9), Art-No.

DANIEL, THOMAS L 1983 Mechanics and energetics of medusan jet propulsion. *Canadian Journal of Zoology* **61** (6), 1406–1420.

DEMONT, M EDWIN & GOSLINE, JOHN M 1988 Mechanics of jet propulsion in the hydromedusan jellyfish, *polyorchis pexicillatus*: Iii. a natural resonating bell; the presence and importance of a resonant phenomenon in the locomotor structure. *Journal of Experimental Biology* **134** (1), 347–361.

FALGOUT, ROBERT D & YANG, ULRIKE MEIER 2002 hypre: A library of high performance preconditioners. In *Computational Science ICCS 2002*, pp. 632–641. Springer.

FAUCI, LISA J & PESKIN, CHARLES S 1988 A computational model of aquatic animal locomotion. *Journal of Computational Physics* **77** (1), 85–108.

GEMMELL, BRAD J, COLIN, SEAN P & COSTELLO, JOHN H 2017 Widespread utilization of passive energy recapture in swimming medusae. *bioRxiv* p. 178467.

GEMMELL, BRAD J, COLIN, SEAN P, COSTELLO, JOHN H & DABIRI, JOHN O 2015 Suction-based propulsion as a basis for efficient animal swimming. *Nature communications* **6**.

GEMMELL, BRAD J, COSTELLO, JOHN H & COLIN, SEAN P 2014 Exploring vortex enhancement and manipulation mechanisms in jellyfish that contributes to energetically efficient propulsion. *Communicative & integrative biology* **7** (4).

GEMMELL, BRAD J, COSTELLO, JOHN H, COLIN, SEAN P, STEWART, COLIN J, DABIRI, JOHN O, TAFTI, DANESH & PRIYA, SHASHANK 2013 Passive energy recapture in jellyfish contributes to propulsive advantage over other metazoans. *Proceedings of the National Academy of Sciences* **110** (44), 17904–17909.

GRIFFITH, BE & LUO, X 2017 Hybrid finite difference/finite element immersed boundary method. *International journal for numerical methods in biomedical engineering* .

HAMLET, CHRISTINA, SANTHANAKRISHNAN, ARVIND & MILLER, LAURA A 2011 A numerical study of the effects of bell pulsation dynamics and oral arms on the exchange currents generated by the upside-down jellyfish *cassiopea xamachana*. *The Journal of experimental biology* **214** (11), 1911–1921.

HERSCHLAG, GREGORY & MILLER, LAURA 2011 Reynolds number limits for jet propulsion: A numerical study of simplified jellyfish. *Journal of theoretical biology* **285** (1), 84–95.

HOOVER, ALEXANDER & MILLER, LAURA 2015 A numerical study of the benefits of driving jellyfish bells at their natural frequency. *Journal of theoretical biology* **374**, 13–25.

HOOVER, ALEXANDER P, GRIFFITH, BOYCE E & MILLER, LAURA A 2017a Quantifying performance in the medusan mechanospace with an actively swimming three-dimensional jellyfish model. *Journal of Fluid Mechanics* **813**, 1112–1155.

HOOVER, ALEXANDER P, TYTELL, ERIC, CORTEZ, RICARDO & FAUCI, LISA 2017b Quantifying performance in the medusan mechanospace with an actively swimming three-dimensional jellyfish model. *Submitted to Journal of Fluid Mechanics* .

HORNUNG, RICHARD D, WISSINK, ANDREW M & KOHN, SCOTT R 2006 Managing complex data and geometry in parallel structured amr applications. *Engineering with Computers* **22** (3–4), 181–195.

HORRIDGE, GA 1954 The nerves and muscles of medusae i. conduction in the nervous system of *aurellia aurita lamarck*. *Journal of Experimental Biology* **31** (4), 594–600.

HUANG, WEI-XI & SUNG, HYUNG JIN 2009 An immersed boundary method for fluid–flexible structure interaction. *Computer methods in applied mechanics and engineering* **198** (33), 2650–2661.

HYPRE 2011 hypre: High performance preconditioners. <http://www.llnl.gov/CASC/hypre>.

IBAMR 2014 IBAMR: An adaptive and distributed-memory parallel implementation of the immersed boundary method. <http://ibamr.googlecode.com/>.

JONES, SK, LAURENZA, R, HEDRICK, TYSON L, GRIFFITH, BOYCE EUGENE & MILLER, LAURA A 2015 Lift vs. drag based mechanisms for vertical force production in the smallest flying insects. *Journal of theoretical biology* **384**, 105–120.

KIRK, B. S., PETERSON, J. W., STOGNER, R. H. & CAREY, G. F. 2006 **libMesh**: A C++ Library for Parallel Adaptive Mesh Refinement/Coarsening Simulations. *Engineering with Computers* **22** (3–4), 237–254, <http://dx.doi.org/10.1007/s00366-006-0049-3>.

MCHENRY, MATTHEW J & JED, JASON 2003 The ontogenetic scaling of hydrodynamics and

swimming performance in jellyfish (*aurelia aurita*). *Journal of Experimental Biology* **206** (22), 4125–4137.

540 MEGILL, WILLIAM MACDONALD 2002 The biomechanics of jellyfish swimming. PhD thesis, The University of British Columbia.

MEGILL, WILLIAM M, GOSLINE, JOHN M & BLAKE, ROBERT W 2005 The modulus of elasticity of fibrillin-containing elastic fibres in the mesoglea of the hydromedusa *polyorchis penicillatus*. *Journal of Experimental Biology* **208** (20), 3819–3834.

545 MILLER, LAURA A & PESKIN, CHARLES S 2004 When vortices stick: an aerodynamic transition in tiny insect flight. *Journal of Experimental Biology* **207** (17), 3073–3088.

MILLER, LAURA A & PESKIN, CHARLES S 2005 A computational fluid dynamics of clap and fling in the smallest insects. *Journal of Experimental Biology* **208** (2), 195–212.

MILLER, LAURA A & PESKIN, CHARLES S 2009 Flexible clap and fling in tiny insect flight. 550 *Journal of Experimental Biology* **212** (19), 3076–3090.

MITTAL, RAJAT & IACCARINO, GIANLUCA 2005 Immersed boundary methods. *Annu. Rev. Fluid Mech.* **37**, 239–261.

PARK, SUNG GOON, CHANG, CHEONG BONG, HUANG, WEI-XI & SUNG, HYUNG JIN 2014 Simulation of swimming oblate jellyfish with a paddling-based locomotion. 555 *Journal of Fluid Mechanics* **748**, 731–755.

PESKIN, CHARLES S 1977 Numerical analysis of blood flow in the heart. *Journal of computational physics* **25** (3), 220–252.

PESKIN, CHARLES S 2002 The immersed boundary method. *Acta numerica* **11**, 479–517.

560 RAMANANARIVO, SOPHIE, GODOY-DIANA, RAMIRO & THIRIA, BENJAMIN 2011 Rather than resonance, flapping wing flyers may play on aerodynamics to improve performance. *Proceedings of the National Academy of Sciences* **108** (15), 5964–5969.

SAHIN, MEHMET & MOHSENI, KAMRAN 2009 An arbitrary lagrangian–eulerian formulation for the numerical simulation of flow patterns generated by the hydromedusa *aequorea victoria*. *Journal of Computational Physics* **228** (12), 4588–4605.

565 SAHIN, MEHMET, MOHSENI, KAMRAN & COLIN, SEAN P 2009 The numerical comparison of flow patterns and propulsive performances for the hydromedusae *sarsia tubulosa* and *aequorea victoria*. *Journal of Experimental Biology* **212** (16), 2656–2667.

SAMRAI 2007 SAMRAI: Structured Adaptive Mesh Refinement Application Infrastructure. <http://www.llnl.gov/CASC/SAMRAI>.

570 SCHMIDT-NIELSEN, KNUT 1972 Locomotion: energy cost of swimming, flying, and running. *Science* **177** (4045), 222–228.

TYTELL, ERIC D, HSU, CHIA-YU, WILLIAMS, THELMA L, COHEN, AVIS H & FAUCI, LISA J 2010 Interactions between internal forces, body stiffness, and fluid environment in a neuromechanical model of lamprey swimming. 575 *Proceedings of the National Academy of Sciences* **107** (46), 19832–19837.

TYTELL, ERIC D, LEFTWICH, MEGAN C, HSU, CHIA-YU, GRIFFITH, BOYCE E, COHEN, AVIS H, SMITS, ALEXANDER J, HAMLET, CHRISTINA & FAUCI, LISA J 2016 Role of body stiffness in undulatory swimming: Insights from robotic and computational models. *Physical Review Fluids* **1** (7), 073202.

580 VIDELER, JOHN J 1993 *Fish swimming*, , vol. 10. Springer Science & Business Media.

ZHANG, CALVIN, GUY, ROBERT D, MULLONEY, BRIAN, ZHANG, QINGHAI & LEWIS, TIMOTHY J 2014 Neural mechanism of optimal limb coordination in crustacean swimming. *Proceedings of the National Academy of Sciences* **111** (38), 13840–13845.

585 ZHAO, HONG, FREUND, JONATHAN B & MOSER, ROBERT D 2008 A fixed-mesh method for incompressible flow–structure systems with finite solid deformations. *Journal of Computational Physics* **227** (6), 3114–3140.